Journal of Materials Chemistry A

Selenium Infiltrated Hierarchical Hollow Carbon Spheres Display Rapid Kinetics and Extended Cycling as Lithium Metal Battery (LMB) Cathodes

Journal:	*Journal of Materials Chemistry A*
Manuscript ID	TA-ART-06-2021-004705.R1
Article Type:	Paper
Date Submitted by the Author:	27-Jul-2021
Complete List of Authors:	Wang, Yixian; University of Texas at Austin, Materials Science and Engineering Program & Texas Materials Institute; The University of Texas at Austin Hao, Hongchang; University of Texas at Austin, Materials Science and Engineering Program & Texas Materials Institute Hwang, Sooyeon; Brookhaven National Laboratory, Center for Functional Nanomaterials Liu, Pengcheng; University of Texas at Austin, Materials Science Program and Texas Materials Institute (TMI) Xu, Yixin; Brookhaven National Laboratory, Center for Functional Nanomaterials Boscoboinik, Jorge; Brookhaven National Laboratory, Center for Functional Nanomaterials Datta, Dibakar; New Jersey Institute of Technology (NJIT), Department of Mechanical and Industrial Engineering Mitlin, David; The University of Texas at Austin

Selenium Infiltrated Hierarchical Hollow Carbon Spheres Display Rapid Kinetics and Extended Cycling as Lithium Metal Battery (LMB) Cathodes

Yixian Wang*[1], Hongchang Hao[1], Sooyeon Hwang[2], Pengcheng Liu[1], Yixin Xu[2,3], J. Anibal Boscoboinik[2], Dibakar Datta[4], David Mitlin*[1]

[1] Materials Science and Engineering Program & Texas Materials Institute (TMI), The University of Texas at Austin, Austin, TX 78712-1591, USA

[2] Center for Functional Nanomaterials, Brookhaven National Laboratory, Upton, NY 11973, USA

[3] Department of Materials Science and Chemical Engineering, State University of New York at Stony Brook, Stony Brook, NY 11794, USA

[4] Department of Mechanical and Industrial Engineering, New Jersey Institute of Technology, Newark, New Jersey 07103, United States

*Corresponding authors.

Emails: yixwang@utexas.edu, David.Mitlin@austin.utexas.edu

Abstract

Lithium metal - selenium (Li-Se) batteries offer high volumetric energy but are limited in their cycling life and fast charge characteristics. Here a facile approach is demonstrated to synthesize hierarchically porous hollow carbon spheres that host Se (Se@HHCS) and allow for state-of-the-art electrochemical performance in a standard carbonate electrolyte (1 M $LiPF_6$ in 1:1 EC:DEC). The Se@HHCS electrodes display among the most favorable fast charge and cycling behavior reported. For example, it delivers specific capacities of 442 and 357 mAh g^{-1} after 1500 and 2000 cycles at 5C and 10C, respectively. At 2C, Se@HHCS delivers 558 mAh g^{-1} after 500 cycles, with cycling Coulombic efficiency of 99.9%. Post-mortem microstructural analysis indicates that the structures remain intact during extended cycling. Per GITT analysis, Se@HHCS possesses significantly higher diffusion coefficients in both lithiation and delithiation processes as compared to the baseline. The superior performance of Se@HHCS is directly linked to its macroscopic and nanoscale pore structure: The hollow carbon sphere morphology as well as the remnant open nanoporosity accommodates the 69% volume expansion of the Li to Li_2Se transformation, with the nanopores also providing complementary fast ion diffusion path.

Introduction

The emerging dominance of electric vehicles is motivating the quest for next-generation renewable batteries with increasing energy and power. The state-of-the-art commercial LIBs are based on transition-metal oxide cathodes and graphite anodes and possess specific energy in the range of 250 Wh kg^{-1}. This does not fully satisfy targeted EV range requirements such as 500 km per charge.[1] Lithium metal anodes possess a reversible capacity of 3860 mAh g^{-1} as well as the lowest redox potential (-3.040 V vs. Standard Hydrogen Electrode (SHE)), making them in principle superior to existing graphite - based anodes.[2-6] When coupled with chalcogen cathodes the corresponding batteries could provide much higher theoretical specific energy, for example 2600 Wh kg^{-1} based on Li_2S.[7-9] To date, commercial practicality remains uncertain for Li-O_2 batteries due to stability and lifetime issues,[10-12] while Li-S batteries still face challenges due to polysulfide shuttling and poor energy efficiency.[13-15]

As another element in the chalcogen family, selenium (Se) possesses several promising electrochemical features, including generally more facile reaction kinetics with lithium as compared to the more oft studied sulfur. The theoretical gravimetric capacity of selenium (675 mAh g^{-1}) is lower than that of sulfur (1675 mAh g^{-1}). However the theoretical volumetric capacity of selenium (3253 Ah L^{-1} based on the density of grey Se 4.82 g cm^{-3}) is comparable to that of sulfur (3467 Ah L^{-1} based on the density of α-S 2.07 g cm^{-3}).[16-20] Selenium has superior electrical conductivity (1×10^{-3} S m^{-1} for crystalline, 5×10^{-13} S m^{-1} for amorphous) than sulfur (5×10^{-28} S m^{-1} for amorphous), which can facilitate improved reaction kinetics and increased active material utilization.[21-26] The compatibility of existing commercial battery carbonate - based electrolytes with Li-Se batteries makes them further attractive for practical applications.

In 2012 Abouimrane *et al.* proposed a new class of Se-based cathodes for room temperature lithium and sodium metal batteries.[27] Since then, various Li-Se architectures have been extensively investigated.[28-34] Similar to the Li-S system, obstacles such as electrode degradation due to the large volume changes associated with the Se to Li_2Se conversion reaction and low active material utilization at fast charge pose significant challenges. Remedies to these issues have included encapsulating the active Se into nanostructured carbon hosts that include carbon nanocomposites[35-37], carbon nanosheets[38, 39], carbon nanotubes[40-43], carbon nanofibers[44-49], and various carbon nanospheres.[50-59] Hollow carbon spheres with core-shell structure are beneficial as ion active

material hosts since their large volume allows for high mass loading, while the remaining void space buffers the lithiation/delithiation volume expansion stresses.[54, 58, 60, 61] For example, Hong *et al.* fabricated hollow carbon microspheres encapsulated Se cathode, which subsequently showed high Se loading (~60 wt.%) and good capacity retention (87% after 1000 cycles at 0.5 A g^{-1}).[61] Hierarchical porous carbons containing both micropores and mesopores are promising Se hosts with the multiscale porosity allowing for improved kinetics and cycling stability.[56, 62, 63] The micropores will provide physical confinement of the active species in the form of small molecules, thereby suppressing the generation of high-order electrolyte-soluble intermediates during cycling.[43, 64, 65] In addition, smaller pores can facilitate the formation of a robust and compact solid electrolyte interphase (SEI).[7] By contrast, the mesopores facilitate improved solid-state diffusivity and provide sufficient host volume to achieve high mass loading of active phases.[66-68] The presence of mesopores within an architecture is also associated with increased cycling stability due to the expansion buffering effect. To prepare hollow and hierarchical porous materials complex templating methods are normally employed, including hard templates (*e.g.* silica[21, 50, 55, 58, 66, 69]) and soft templates (*e.g.* polystyrene[60]). A facile fabrication method that can achieve hierarchical microporous - mesoporous distributions within a carbon host is therefore sought.

Herein, we synthesized Hierarchical Hollow Carbon Spheres (HHCS) employing a single-step activation approach, based on select tuning of the ratio between the monodisperse carbon spheres precursor and the activation agent. After melt-infiltration of Se, the Se@HHCS electrode was obtained. As will be demonstrated, this architecture offers highly promising electrochemical performance both in terms of rate capability and extended cyclability.

Experimental

Materials Synthesis.

Monodisperse carbon spheres (MCS) were synthesized through a modified Stöber method with resorcinol and formaldehyde solution as precursors.[70] In a typical synthesis, 0.2 mL ammonia hydroxide (25 wt.%) was added to a solution containing 16 mL anhydrous ethanol and 40 mL deionized (DI) water and mixed at room temperature (RT) with magnetic stirring for 1 h. In the next step, 0.4 g resorcinol was dissolved in the solution and continually stirred for another 0.5 h.

Subsequently, 0.6 mL formaldehyde solution was added and stirred for 24 h under RT. The solution gradually became turbid. The resultant colloid was then transferred to a 100 mL Teflon-lined hydrothermal reactor and maintained at 100 ^{o}C for 24 h to promote the polymerization.[70] Afterwards, the milky-white colloidal solution turned clear with brick-red precipitation at the bottom, indicating an enhancement of the polymerization after hydrothermal treatment. The resorcinol-formaldehyde polymer resin was collected though vacuum filtration, washed by DI water and ethanol for several times, and subsequently dried at 60 ^{o}C under vacuum overnight. The monodisperse carbon spheres were obtained after curing it for 4 h at 400 ^{o}C in a tube furnace under continuous Ar flow.

The as-obtained spheres were dispersed in 10 mL DI water containing pre-dissolved activation agent (KOH). The ratio between MCS and KOH is controlled to be 1:2 by weight. The slurry was homogenized under ultrasound treatment for 0.5 h and subsequently dried in a convection oven at 80 ^{o}C overnight. The flakes were then ground to fine powder and transferred to a tube furnace where they were annealed at 700 ^{o}C for 2 h under a constant Ar flow. The resultant carbonized product was treated with 1 M hydrochloric acid (HCl) to remove the salts. Hierarchical hollow carbon spheres (HHCS) were generated after collecting the precipitates from the solution. To prepare control samples, similar approaches were carried out with different amount of KOH addition. The ratios between MCS and KOH were set to be 1:1 and 1:3 to synthesize microporous carbon spheres (MPCS) and microporous carbon particles (MPCP), both of which were tested as baselines. The carbon hosts (HHCS, MPCS and MPCP) were mixed with commercial Se powder at a ratio of 1:1 by weight and homogenized for 0.5 h using a mortar and pestle. The mixture was then sealed in a stainless-steel autoclave reactor held at 260 ^{o}C for 12 h while under argon. The final selenium - carbon sphere composites were collected after cooling down to room temperature, being denoted as Se@HHCS (primary material), Se@MPCS (baseline) and Se@MPCP (baseline). To achieve high selenium mass loading in HHCS, HHCS and Se powder were mixed at a weight ratio of 1:2, followed by the same approach as described above. The high mass loading specimen is denoted as "Se_{HL}@HHCS".

Materials Characterization.

The morphology, structure and composition of the carbons were analyzed by scanning electron microscopy (SEM, Hitachi S-5500) and transmission electron microscopy (TEM, JEOL 2100F

and FEI Talos F200X), both equipped with an energy dispersive X-ray spectroscopy (EDXS) detector. X-ray diffraction (XRD) analysis was performed on Rigaku Miniflex 600 diffractometer with Cu Kα radiation (λ = 1.54178 Å) at a scan rate of 5° per minute within the 2θ range from 10° to 80°. Nitrogen adsorption-desorption profiles were recorded at 77 K using Quantachrome Autosorb IQ analyzer. X-ray photoelectron spectroscopy (XPS) results were collected on a customized XPS system based on a Hemispherical Energy Analyzer PHOIBOS 100 (SPECS Surface Nano Analysis GmbH) with Mg Kα as the excitation sources. Thermogravimetric analysis (TGA) data was collected on Mettler Thermogravimetric Analyzer under N_2 flow from room temperature to 1000 °C at a ramp of 10 °C min^{-1}.

Electrochemical Measurements.

Electrochemical tests were carried out using CR2032 coin cells assembled in an Ar-filled glove box ($O_2 \leq 0.1$ppm, $H_2O \leq 0.1$ppm). The working electrodes were prepared by mixing the active materials, Super P and polyvinylidene difluoride (PVDF) binder at a weight ratio of 8:1:1 in N-methyl-2-pyrrolidone (NMP) solvent to form a homogenous slurry. It was subsequently coated onto aluminum foil current collectors and dried in a vacuum oven at 60 °C for 12 h. In the "standard" array of tests, the mass loading of each electrode was around 1.5 mg cm^{-2}. Higher mass loading analyses were also performed, with mass loadings up to 4.5 mg cm^{-2}. To assemble Li-Se cells, round lithium foils (MTI) were used as both counter and reference electrode, while porous polypropylene (PP) was used as the separator. The electrolyte consisted of 1 M $LiPF_6$ dissolved in ethylene carbonate (EC) and diethylene carbon (DEC), with a volume ratio of 1:1. The galvanostatic discharge/charge rate and cycling performances of Se@C composites were evaluated on Wuhan LAND-CT2001A battery testers within a potential window of 1.0-3.0 V vs. Li/Li^+. Cyclic voltammetry (CV) profiles were recorded between 1.0-3.0 V at scan rates ranging from 0.1 to 1.2 mV s^{-1}. Electrochemical impedance spectroscopy (EIS) was measured at the frequency range of 100 kHz to 10 mHz, with an amplitude of 10 mV. The galvanostatic intermittent titration technique (GITT) was carried out under a constant pulse current of 0.05C for 0.5 h, followed by a 4 h relaxation. Prior to the GITT analysis, cells were pre-activated for 5 cycles on Land battery testers. The EIS and GITT measurements were performed on Princeton Applied Research VersaSTAT 4 electrochemical workstations. All electrochemical analysis was performed at room temperature.

Results and Discussion

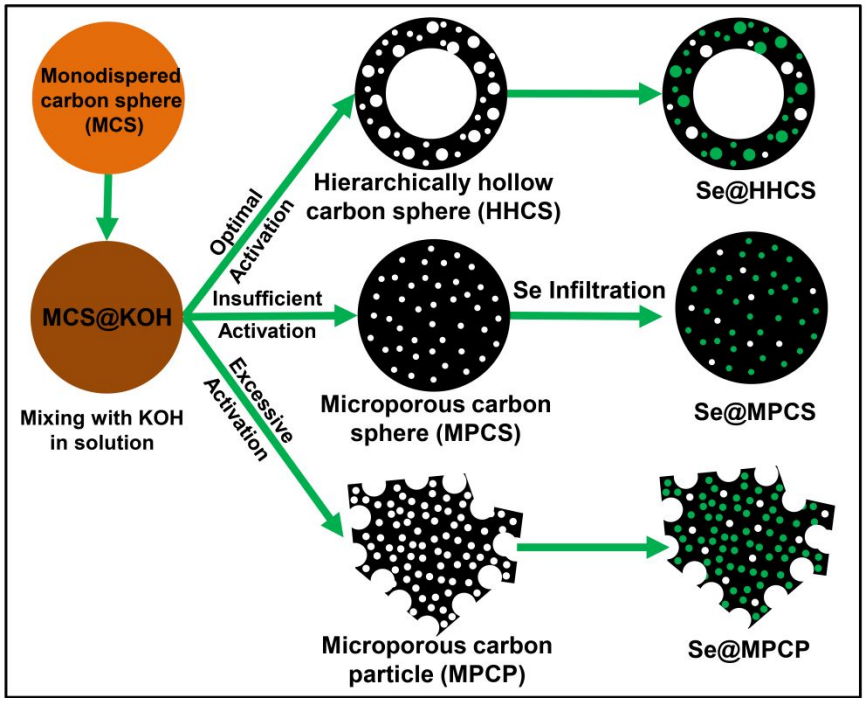

Schematic 1. Illustration of the preparation processes and the structure of Se@HHCS, Se@MPCS and Se@MPCP.

Schematic 1 illustrates the fabrication processes and the associated structure of Se@HHCS (primary material), Se@MPCS (baseline) and Se@MPCP (baseline). In summary, monodispersed carbon spheres (MCS) with an average diameter of 680 nm were synthesized using a modified Stöber method and were subsequently mixed with the activation agent (KOH) at different ratios in a liquid medium. Scanning electron microscope images and the associated size distribution of the MCS are shown in **Figure S1**. The liquid mixing approach enabled a better dispersion and impregnation of the activation agent, allowing a more uniform distribution of KOH throughout the MCS precursors. The homogenous mixture was obtained after drying and subject to an annealing process, during which both activation and carbonization processes occurred. The precursor reacted with KOH under inert atmosphere while evolving gaseous products *e.g.* CO, CO_2, H_2 and H_2O, resulting in morphology evolution and the formation of multidimensional porosity.[71, 72] KOH activation is an atomically site-specific attack, preferentially eliminating the more volatile portions of the carbon.[73] During the curing of RF polymer resin spheres, the outer shell undergoes more extensive polymerization as compared with the inside core. This is due to the difficulty of eliminating the volatile species from the inside of the particles and possible localized temperature

gradients. As a result, the inner core of the spheres is left less chemically stable. During subsequent KOH activation, the less cured resin core is extensively attacked, forming the hollow structure. As the relative content of KOH is increased, the reaction becomes more aggressive and ultimately the entire particle is heavily corroded. To achieve the targeted hierarchical hollow carbon spheres (HHCS), an optimal MCS to KOH weight ratio was determined to be 1:2. A lower KOH content leads to the inner core surviving and mesopores not being formed. These were the microporous carbon spheres (MPCS) tested as a baseline. A higher KOH content completely destroyed the spherical structure, forming the microporous carbon particles (MPCP). Interestingly excessive KOH did not result in mesopores. Likely the regions of the carbon where mesopores could have formed were so drastically attacked that macropores were formed instead, resulting in block-like rather than spherical morphologies. Selenium was melt infiltrated into the three carbons using identical heat treatment conditions. The resultant architectures Se@HHCS, Se@MPCS and Se@MPCP served as the cathodes for Li-Se batteries. As discussed in the experimental, high mass loading specimens Se_{HL}@HHCS were also fabricated and tested.

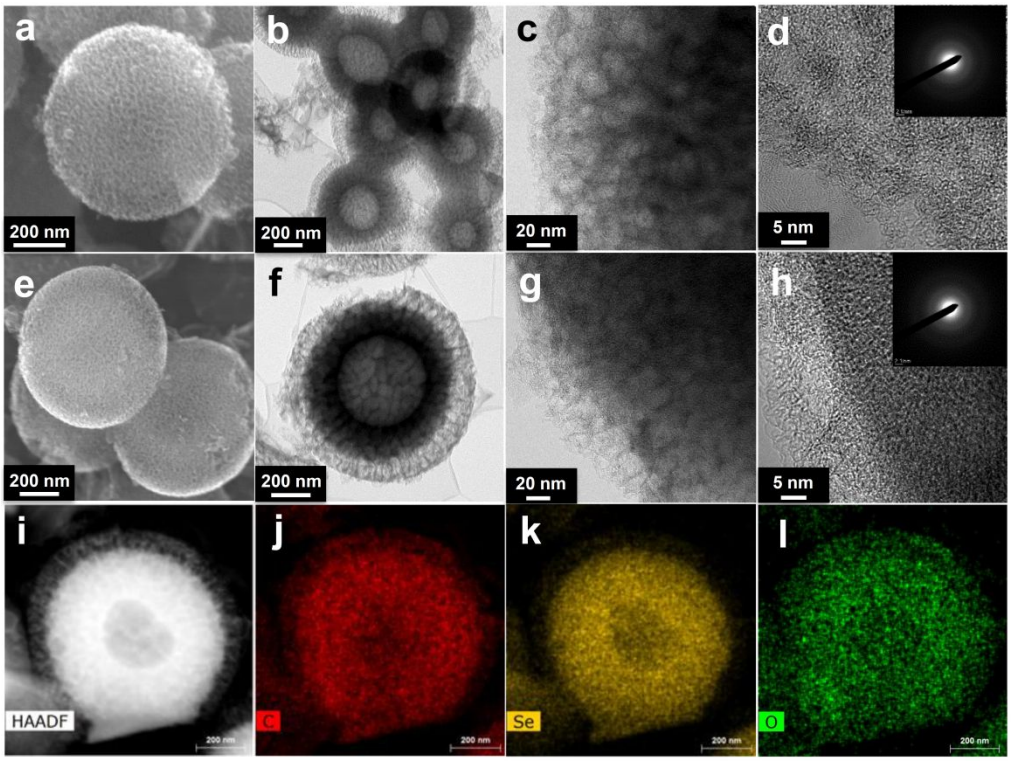

Figure 1. (a) SEM image of HHCS carbon host, **(b)** - **(d)** TEM images with associated SAED insets and HRTEM images of HHCS **(e)** SEM image of Se@HHCS. **(f)** - **(h)** TEM and HRTEM images of Se@HHCS. **(i)** - **(l)** TEM HAADF image and associated EDXS maps of C, Se and O, respectively for Se@HHCS. Analogous analysis for baseline samples MPCS, Se@MPCS, MPCP and Se@MPCP is shown in the Supplemental.

The morphology, structure and chemistry of the materials were analyzed by scanning electron microscopy (SEM) and transmission electron microscopy (TEM). **Figure 1(a)** displays SEM image of the HHCS hosts, the unfilled carbon spheres displaying a roughened surface due the activation process. Low magnification SEM images and the associated size distribution of the HHCS are shown in **Figures S2 (a) - (b)**. The average diameter of the HHCS sphere was 815 nm, taken from a stereology analysis of 52 spheres total. **Figures 1(b) - (d)** display analysis of HHCS, showing TEM images with associated selected area electron diffraction (SAED) insets and high-resolution TEM (HRTEM) images. The hollow core morphology of the spheres is clearly discernable from the bright field contrast. The higher magnification TEM image in **Figure 1(c)** displays variations in mass-thickness contrast synonymous with mesopores, although the specimen is thick enough where the individual pores cannot be directly imaged due to overlap with the carbon. According to the associated SAED pattern and HRTEM image in **Figure 1(d)**, the carbon structure is highly disordered with no evidence of intact graphene planes. **Figures 1(f) - (h)** show TEM and HRTEM images of Se@HHCS, highlighting the amorphous structure of Se that fills the nanopores but not the hollow core of HHCS. **Figures 1(i) - (l)** show scanning TEM high-angle annular dark-field (STEM-HAADF) images and associated energy dispersive X-ray spectroscopy (EDXS) maps of C, Se and O, also illustrating the uniform dispersion of Se within the nanopores.

Figure S3(a) displays an SEM image of the MPCS hosts, the unfilled carbon spheres displaying a relatively smooth surface. Low magnification SEM images and the associated size distribution of the MPCS are shown in **Figures S2(c) - (d)**. The average diameter of the MPCS sphere was 624 nm, taken from a stereology analysis of 97 spheres total. **Figures S3(b) - (d)** display analysis of MPCS, showing TEM images with associated SAED insets and HRTEM images. It may be observed that the structure of the spheres is disordered, similar to HHCS. However, the spheres display neither the contrast associated with a hollow core, nor the contrast associated with mesoporosity. The micropores in the specimen overlap with the carbon and cannot be resolved in the HRTEM image. **Figure S3(e)** displays an SEM image of the of the MPCP hosts, which are no longer spherical at all. Rather the resultant carbon hosts are a series of large irregularly particulates with concave surfaces that appear as a series of shallow macropores. As it will be demonstrated, these specimens also contain microporosity but are relatively free of mesopores. The MPCP materials also do not contain a hollow inner core.

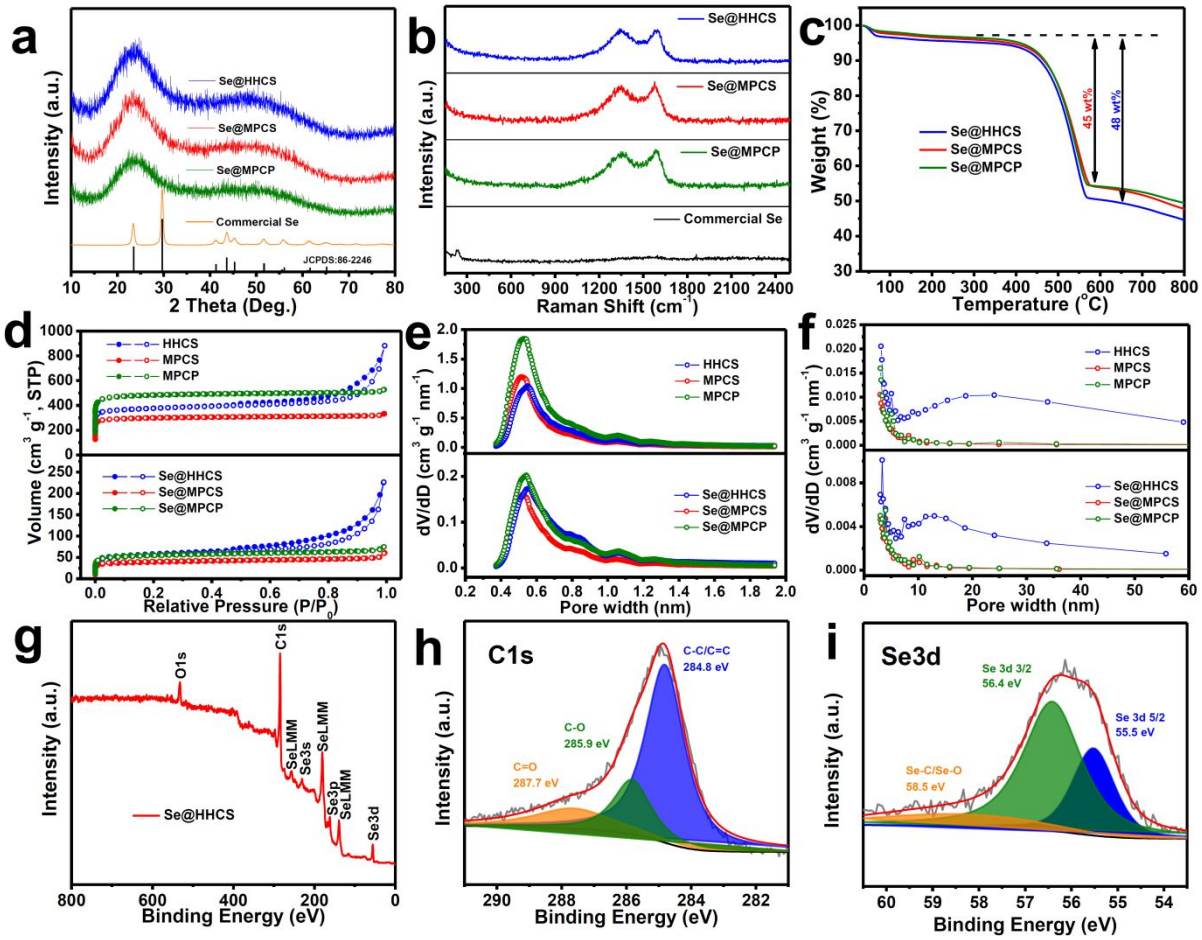

Figure 2. Analytical characterization of Se@HHCS, and baseline Se@MPCS, Se@MPCP. **(a)** Indexed XRD patterns **(b)** Raman spectra including as-received commercial Se powder. **(c)** TGA curves from room temperature to 800 °C, tested in Ar. **(d)** - **(f)** Nitrogen absorption-desorption isotherms, Horvath-Kawazoe (HK) pore size distributions and Barrett-Joyner-Halenda (BJH) pore size distributions of the as-synthesized samples. **(g)** - **(i)** XPS Survey spectrum and high resolution XPS spectra of C1s and Se3d of Se@HHCS.

The structure of the three Se-infiltrated carbons was further analyzed by X-ray diffraction (XRD), as shown in **Figure 2(a)**. Baseline as-received commercial Se powder is crystalline with a hexagonal $P3_121$ space group (a = b = 4.368 Å, c = 4.958 Å, JCPDS #86-2246). After Se is impregnated into the three carbon hosts, all characteristic crystalline peaks disappear. Instead, the XRD patterns are characteristic of amorphous materials, with a broad hump centered near $2\theta = 23^{o}$ and the corresponding broadened second order peak at 46°. The second order peak displays some splitting (most prominent in the Se@MPCP), indicating that the amorphous Se and amorphous carbon near-neighbor peaks overlap.[24] The same conclusion about the disordered structure of both the carbon host and of Se can also be drawn from the Raman analysis shown **Figure 2(b)**. The

pristine Se displays one characteristic peak at ~236 cm^{-1}, corresponding to the chain-like Se.[16, 40, 74] However, no obvious Se peaks are present in the three specimens. The two peaks at 1350 and 1590 cm^{-1} are associated with D-band and G-bands of the carbons.[75, 76] The intensity ratio of D-band to G-band (I_D/I_G) is approaching 1 for all specimens, demonstrating disordering in the carbon hosts and agreement with the XRD findings. **Figure 2(c)** shows the thermogravimetric analysis (TGA) curves indicating that the Se mass loading was 48 wt.% in Se@HHCS and was 45 wt.% in both Se@MPCS and Se@MPCP. Selenium loading of 64 wt.% was obtained with Se_{HL}@HHCS, as shown in **Figure S4(a)**. Per **Table S1**, this high mass loading compares favorably with values obtained for state-of-the materials published prior.

Table 1. Textural properties of the as-synthesized carbons.

Sample	S_{BET}[a] (m^2 g^{-1})	V_{tot}[b] (cm^3 g^{-1})	V_{mic}[c] (cm^3 g^{-1})	V_{mes}[d] (cm^3 g^{-1})	V_{mes}/V_{tot}
HHCS	1491	1.074	0.574	0.500	0.466
MPCS	1202	0.493	0.457	0.036	0.007
MPCP	1928	0.793	0.739	0.054	0.007
Se@HHCS	203	0.251	0.082	0.169	0.673
Se@MPCS	149	0.078	0.059	0.019	0.243
Se@MPCP	209	0.105	0.082	0.023	0.219
Se_{HL}@HHCS	26	0.081	0.008	0.073	0.901

[a]BET specific surface area.

[b]Total pore volume.

[c]Micropore volume.

[d]Mesopore volume.

To investigate the textural properties of the specimens, N_2 adsorption-desorption experiment was performed at 77 K. The resulting isotherms are shown in **Figure 2(d)**. HHCS exhibits a type IV isotherm with H3 hysteresis loop according to the IUPAC classification, which is associated with the multilayer adsorption followed by capillary condensation in the mesopores.[77] By contrast, both MPCS and MPCP display type I isotherms, indicating their microporous structure. All samples show a dramatic increase of N_2 adsorption at $P/P_0 < 0.01$, indicating the presence of a

great amount of micropores. The calculated Brunauer-Emmett-Teller (BET) surface areas of HHCS, MPCS and MPCP are 1491, 1202 and 1928 $m^2 g^{-1}$, respectively. The calculated total pore volume (TPV), however, displays a distinct trend as shown in **Table 1**. The HHCS sample not only has the largest TPV (1.074 $cm^3 g^{-1}$) compared to that of MPCS (0.493 $cm^3 g^{-1}$) and MPCP (0.793 $cm^3 g^{-1}$), but it also possesses the largest mesopore volume, which contributes to almost half of the TPV. In contrast, micropores are dominant in both MPCS and MPCP with contributions of 92.7% and 93.2% to the TPV, respectively.

To gain further insight regarding the textural properties of the hosts, Horvath-Kawazoe (HK) and Barrett-Joyner-Halenda (BJH) pore size distributions are plotted in **Figures 2(e) and 2(f)**, respectively. This allows for analysis of micropores and mesopores separately. The three specimens display similar size distribution in terms of micropores with the peak in the differential volume being centered at 0.52 nm. Those results are illustrated in **Figure 2(e)**. The main difference is found in the mesopore range where HHCS possesses significantly more mesopores than the other two carbons, per **Figure 2(f)**. HHCS has a broad distribution of pores ranging from 10-50 nm with the distribution peak being situated at 20 nm. This is in accordance with scale of the "pore-like" contrast variation in the TEM observations. After Se infiltration, there is a dramatic reduction of surface area, per **Figure 2(d)** and **Table 1**. In fact, the majority (not all) of the nitrogen accessible porosity is sealed off. The HK and BJH pore size distributions for Se@HHCS, Se@MPCS and Se@MPCP show similar results to the unfilled hosts, with Se@HHCS exhibiting a much higher volume uptake of mesopores. The statistical data of the mesopore volume contribution to the TPV are listed in **Table 1,** where mesopores account for 67.3% of the TPV of Se@HHCS, versus 24.3% for Se@MPCS and 21.9% for Se@MPCP. The total open pore volume of the Se@HHCS, Se@MPCS and Se@MPCP specimens is 0.251 $cm^3 g^{-1}$, 0.078 $cm^3 g^{-1}$ and 0.105 $cm^3 g^{-1}$, respectively. Per **Figure S4(b)** with the higher Se loading in Se_{HL}@HHCS, both the remnant surface area and the remnant pore volume are reduced to 26 $m^2 g^{-1}$ and 0.081 $cm^3 g^{-1}$, respectively. However 90% of this pore volume is due to mesopores, and should therefore still be useful for enhancing the reaction kinetics and buffering the lithiation volume expansion.

X-ray photoelectron spectroscopy (XPS) was conducted to investigate the chemical compositions and surface functional groups in Se@HHCS, which was the target material. Based on the XPS survey spectrum shown in **Figure 2(g)**, the only impurity being detectable in

Se@HHCS is oxygen with a content of 3.9 at.%. The high-resolution C 1s spectrum in **Figure 2(h)** displays the dominant peak located at 284.8 eV, which corresponds to the C-C bonds in both the host and the adventitious carbon. The peaks situated at 285.9 and 287.7 eV are ascribed to C-O and C=O species, respectively. In the Se 3d spectrum shown in **Figure 2(i)**, the peaks at 55.5, 56.4 and 58.5 eV are attributed to the Se $3d_{5/2}$, Se $3d_{3/2}$ and Se-C/Se-O, respectively.

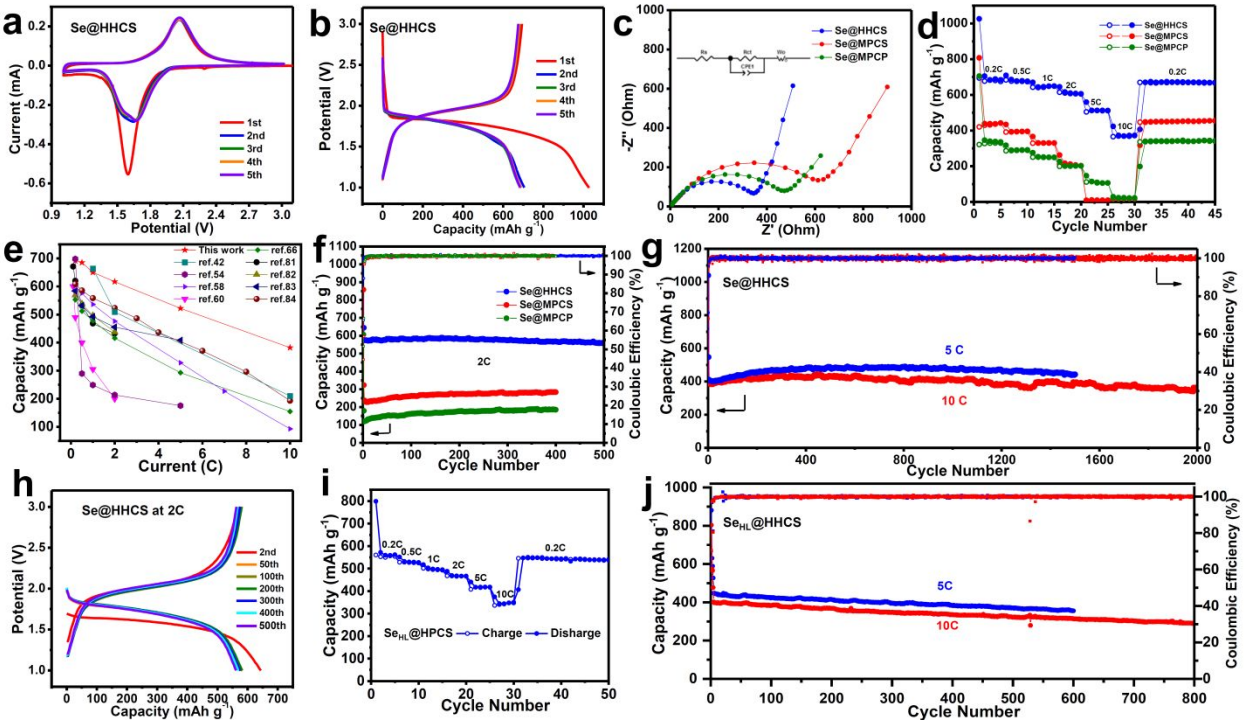

Figure 3. Electrochemical performance of Se@HHCS, and baseline Se@MPCS, Se@MPCP. **(a)** CV curves of Se@HHCS at 0.1 mV s^{-1} for the first 5 cycles. **(b)** Galvanostatic profiles of Se@HHCS at 0.2C (1C = 675 mAg^{-1}). **(c)** Nyquist plots of the three electrodes prior to cycling. **(d)** Rate capability comparison for the three materials. **(e)** Rate capability comparison of Se@HHCS with Se-based cathodes in published literature. **(f)** Comparison of the cycling performance of the three electrodes at 2C. **(g)** Cycling performance of Se@HHCS at 5C and 10C. **(h)** Galvanostatic profiles of Se@HHCS at 2C after 2nd, 50th, 100th, 200th,300th, 400th and 500th cycles. **(i), (j)** Rate capability and cycling performance of Se_{HL}@HHCS.

The electrochemical performances of the as-synthesized Se@C composites were evaluated in half-cell configurations, employing lithium metal foil as the anode and a conventional polypropylene (PP) separator. An electrolyte of 1 M $LiPF_6$ in EC/DEC by a volume ratio of 1:1 was used without any additives. Cyclic voltammetry (CV) analysis was performed in the window of 1.0-3.0 V vs Li/Li^+. **Figure 3(a)** shows the CV curves of the Se@HHCS electrode in the first 5 cycles at a scan rate of 0.1 mV s^{-1}. During the first cathodic process, a single large reduction peak

centered at 1.60 V is present, which corresponds to a combination of irreversible SEI formation and the initial reversible reduction of Se to Li_2Se. The cathodic peak shifts to be centered at 1.66 V in the subsequent cycles with an attenuated intensity, which is expected since SEI primarily forms at cycle 1. After the first cathodic scan, there is also some capacity loss due to the Li irreversibly adsorbing at high binding energy defect sites in the carbon lattice.[56] During the anodic scans there is a single oxidation peak centered at 2.06 V that does not shift in its center with cycling. From cycle 2 onwards, the single pair of redox peaks is correlated to the direct phase transition between selenium and Li_2Se without the formation of intermediate polyselenide species.[7, 22, 78, 79] There is consistent peak overlap at each cycle number, indicating that the steady-state redox processes do not increase their associated overpotential or are otherwise affected. The CV curves of Se@MPCS and Se@MPCP are shown in **Figure S5.** While qualitatively these materials display similar trends, the separation of the redox peaks is greater than that for Se@HHCS, indicating larger polarization for both systems. Moreover, the peak centers diverge further event for cycles 1 - 5, indicating increasing overpotentials with cycling, the cause being discussed in more detail subsequently.

Post-mortem XRD and XPS were carried out to understand the lithiation products and the SEI structure after the 1st discharge (lithiation) to 1 V of Se@HHCS. Per **Figure S6**, the Bragg diffraction peaks corresponding to equilibrium *fcc* Li_2Se (Fm-3m, No. 225, a = b = c = 0.6002 nm) are observed, demonstrating this to be the terminal phase. The XPS spectra presented in **Figure S7** demonstrates that the SEI consists of both organic and inorganic components, as expected. The high-resolution C1s spectrum shown in **Figure S7(a)** consists of four individual peaks, corresponding to C-C (284.8 eV), C-O (286.6 eV), C=O (288.1 eV) and O-C=O (289.8 eV). The high-resolution F1s and P2p spectra in **Figures S7(b) and S7(c)** indicate the existence of Li_xPF_y, $Li_xPF_yO_z$ and LiF, which has been ascribed to the decomposition of PF_6^- anions on the electrode surface.[7, 64] As shown in **Figure S7(d)**, the Se3d signal is shifted to a lower binding energy versus the unreacted baseline, with $Se3d_{5/2}$ and $Se3d_{3/2}$ situated at 53.5 and 54.4 eV. This agrees with the reduction of Se to Li_2Se.[7]

Figure 3(b) and **Figure S8** show the galvanostatic profiles of Se@HHCS, Se@MPCS and Se@MPCP cathodes measured at a current density of 0.2C (1C = 675 mAh g^{-1}, *i.e.* capacity of Li_2Se). The single voltage plateaus in both discharge and charge processes agree well with CV

analyses. The initial discharge/charge specific capacities of Se@HHCS, Se@MPCS, and Se@MPCP are 1026/694, 807/429 and 705/327 mAh g^{-1}, corresponding to Coulombic efficiencies (CEs) of 67.6%, 53.2% and 46.4%, respectively. The initial discharge capacities of all samples exceed the theoretical capacity of Se (675 mAh g^{-1}), which is a quite common behavior among carbon confined Se cathodes.[7, 38, 80] The extra reversible capacity in Se@HHCS is ascribed to Li storage in HHCS. Per **Figure S9(a)** the reversible capacity of HHCS in the relevant voltage regime is 84 mAh g^{-1}, which would contribute roughly 42 mAh g^{-1} to the total reversible capacity of the electrode. This indicates that the majority of the reversible capacity originates from the Se phase, not the carbon host. The calculated polarization was based on the voltage difference at 50% discharge/charge states. These values are 0.14 V, 0.36 V and 0.42 V for Se@HHCS, Se@MPCS and Se@MPCP, respectively, indicating the enhanced electrochemical kinetics of the Se@HHCS electrode. Volumetric capacity and energy density are of key importance for practical applications where space is limited *e.g.* in electric vehicles. **Figure S10** provides the volumetric capacity and energy density of Se@HHCS tested at 0.2C (after the initial formation cycle). The values are 560 mAh cm^{-3} and 930 Wh L^{-1} (1162 Wh kg^{-1}) based on the mass of Se and the packing density of the electrode (0.8 mg cm^{-3}), respectively. In principle, these numbers can be further improved by increasing the packing density of the electrode on the current collector. To further analyze the three materials, electrochemical impedance spectroscopy (EIS) was carried out. The corresponding Nyquist plots are presented in **Figure 3(c)**. It is evident that Se@HHCS possessed the lowest interfacial resistance among all Se@C samples before cycling. Per **Figure S11**, Se@HHCS maintained the lowest resistance of the three specimens after the 1st and 5th cycle as well.

Figure 3(d) displays a comparison of the rate capability of the three cathodes materials. At every current density, Se@HHCS electrode exhibited the highest specific capacities of the three, with the difference increasing with faster charge. The reversible capacities for Se@HHCS are 691, 685, 650, 617, 522 and 382 mAh g^{-1} at 0.2, 0.5, 1, 2, 5 and 10C, respectively. By contrast, neither the Se@MPCS nor the Se@MPCP cathodes are able to fast charge, with their capacities decreasing to effectively nil at 10C. The Se@HHCS is also structurally stable at high rates: When the current is switched from 10C back to 0.2C, its capacity is restored to the original level. According to **Figure 3(e)**, the rate performance of the Se@HHCS cathode is among the most favorable in literature in terms of capacity retention.[42, 54, 58, 60, 66, 81-84] A key figure of merit is the capacity achieved at realistic charging fast times, such as 1 hour, 30 minutes, 15 minutes, *etc.* It may be

observed that even at the extreme 6 minutes charging time (10C) the capacity retained is quite high.

The exceptional rate performance in Se@HHCS may be attributed to its unique pore structure that differs in fundamental ways from the porosity in Se@MPCS and Se@MPCP, as well as from prior literature reports. As indicated earlier, the total open pore volume of the Se@HHCS, Se@MPCS and Se@MPCP specimens is 0.251, 0.078 and 0.105 $cm^3\ g^{-1}$, respectively. This open nitrogen accessible space should also be accessible to electrolyte, becoming covered with SEI in the process. We propose that this is critical for explaining the differences between the electrochemical performance of the three specimens, and why Se@HHCS is substantially superior. The hollow structure of Se@HHCS certainly helps with the performance, giving the spheres a certain level of elastic flexibility to withstand the lithiation - delithiation induced stresses. However, that is not the entire story, since a hollow structure *per se* does not fully explain the fast charge kinetics. The role of open porosity is critical, since this is the space that accommodates the extra 69 vol% change associated with going from amorphous Se to the *fcc* Li_2Se (density of Li_2Se is 2.83 g/cm^3, of Se is 4.79 g/cm^3). The SEI in and around the pores should be mechanically complaint and would not exert the same level of pushback on the Li_2Se as the carbon host. Without the extra pore space, this volume expansion acts directly against the walls of the carbon, requiring that the structure flexes and/or fractures. The lowest charge - discharge voltage hysteresis with Se@HHCS, as well its overall most favorable kinetics, are explainable by this extra porosity that allows for facile lithiation - delithiation induced expansion - contraction. The extended cyclability is likewise explained since the carbon host is not pulverized or otherwise damaged. The pores in Se@HHCS should acts as fast diffusion paths for Li ions, with fast transport both via the pore penetrating electrolyte and via the SEI - carbon interfaces.

Figure 3(f) compares the cycling performances of the three electrodes, tested at 2C. The associated galvanostatic profiles of these samples are presented in **Figure 3(h)** and **Figure S12**. Se@HHCS displayed the overall best performance, with a capacity of 558 mAh g^{-1} being retained after 500 cycles. By contrast, after 400 cycles the baseline Se@MPCS and Se@MPCP electrodes retained a capacity of 284 mAh g^{-1} and 185 mAh g^{-1}, respectively, with cycling CE's being lower. The average CEs are 99.9% for Se@HHCS, 99.7% for Se@MPCS, 99.6% for Se@MPCP. Per the raw galvanostatic data, both Se@MPCS and Se@MPCP display much larger voltage polarization,

as evidenced by the widely separated discharge and charge curves. The polarization of Se@HHCS remains relatively small and remains constant after cycle 2. Higher mass loading experiments were also conducted to examine the electrochemical performance of the Se@HHCS electrode at more industrially relevant electrode formulations. Electrodes were analyzed at active material mass loadings of 2.5, 3.8 and 4.6 mg cm^{-2}. As can be observed from **Figure S13(a)**, with a mass loading of 2.8 mg cm^{-2}, a reversible capacity of 364 mAh g^{-1} can is retained at a high current of 5C. **Figure 13(b)** shows the cycling results which demonstrate that with a mass loading of 2.5, 3.8 and 4.6 mg cm^{-2}, Se@HHCS delivers capacities of 509, 451, 359 mAh g^{-1} at 1C after 500 cycles. To further demonstrate the fast - charge stability of Se@HHCS, extended cycling was performed at 5C and 10C. This represents a very aggressive testing regiment since there is minima time to relax the stresses associated with the 69 vol% change associated with going from amorphous Se to the *fcc* Li_2Se. As shown in **Figure 3(g)**, the Se@HHCS cathode delivers specific capacities of 442 and 357 mAh g^{-1} after 1500 and 2000 cycles at 5C and 10C, respectively, with both CEs approaching 100%. With a Se mass loading of 64 wt.%, the Se_{HL}@HHCS electrode also displays good rate capability. For example, per **Figure 3(i)** a specific capacity of 352 mAh g^{-1} is obtained at 10C. **Figure 3(j)** shows the cycling performance of Se_{HL}@HHCS. The specimen delivers a reversible capacity of 356 mAh g^{-1} after 600 cycles at 5C, and 290 mAh g^{-1} after 800 cycles at 10C. **Table S1** provides a comparison of the cycling behavior of Se@HHCS versus state-of-the-art Se-based cathodes from literature. It may be concluded that the cycling characteristics of Se@HHCS are among the most favorable.

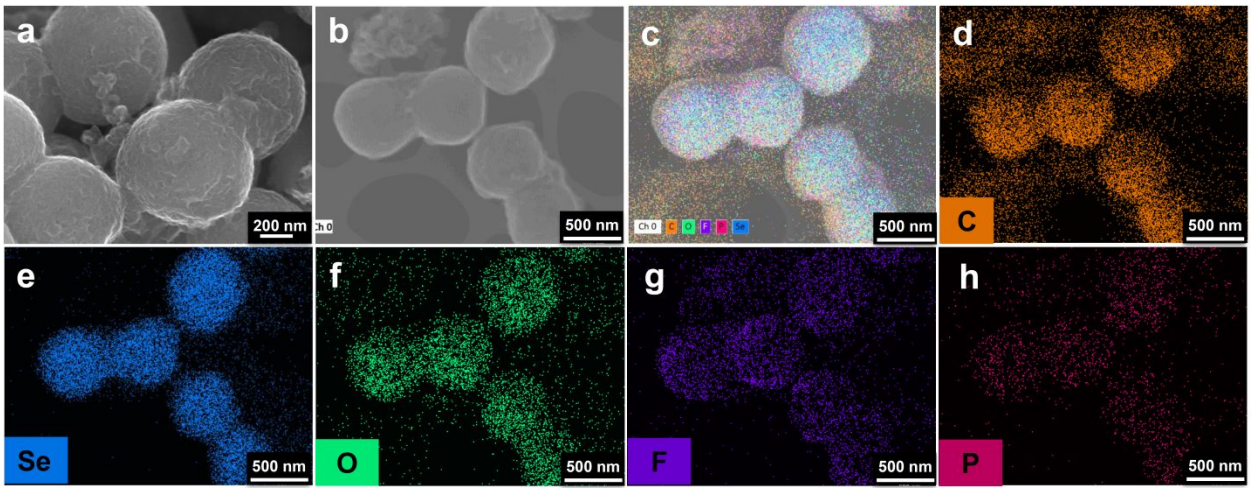

Figure 4. (a) - **(h)** SEM and associated EDXS elemental maps of Se@HHCS electrode after 200 cycles at 2C.

Figure 4(a) confirms that the spherical structure of Se@HHCS electrode after 200 cycles at 2C is geometrically intact, being free from pulverization, agglomeration or other severe volume changes that would impede the kinetics. The figure shows SEM and associated EDXS elemental maps of Se@HHCS, confirming the uniform distribution of Se within the spheres after extended cycling. In addition, its surface is uniformly covered by the SEI layer, which is mainly composed of O, P, and F-containing species as indicated by the EDXS mapping in **Figures 4(b) - (h)**.

Electroanalysis was performed to further understand the kinetics of Se@HHCS versus the Se@MPCS baseline, which possessed a similar morphology but differed in their textural (porosity) properties. The CV curves of Se@HHCS and Se@MPCS were collected at different scan rates (v), ranging from 0.1-1.2 mV s^{-1}. As displayed in **Figures 5(a) and 5(b)**, the cathodic and anodic peaks of both samples gradually shifted upon the increasing the rate, indicating increasing polarization. The dependence of the peak currents on the scan rates can be evaluated based on the relationship $\boldsymbol{i = av^b}$, where i is the peak current, v is the scan rate, $\boldsymbol{a}$ and $\boldsymbol{b}$ are constants to be determined. The characteristic $\boldsymbol{b}$ value ranges from 0.5 to 1.0 and is used to determine the rate limiting process during charge storage for a given scan rate. When the $\boldsymbol{b}$ value approaches 1, indicating a linear relationship of peak current with time, the charge storage process is reaction-controlled, *i.e.* activation polarization limited. Although this is often termed as "surface capacitive process", it does not necessarily represent EDLC charge storage mechanism.[28, 85-90] For electrode materials that are covered by an SEI layer such as Se@HHCS, there is not sufficient electroactive surface area to generate much EDLC current. Rather, for Se@HHCS this reaction-controlled charge storage capacity originates from activation polarization of the lithiation/delithiation reaction Se <=> Li_2Se. While not being EDLC, an activation polarization limited process still occurs at a surface or at an interface, such as at Se-SEI or at Se-carbon interface. With reduced charging rates, the $\boldsymbol{b}$ value approaches 0.5, and the reversible capacity originates progressively more from a process that is solid-state diffusion controlled. A higher fraction of the overall capacity comes from the same Se <=> Li_2Se reaction but "deep inside" the Se@HHCS carbon wall, where it takes time for Li ions to penetrate.

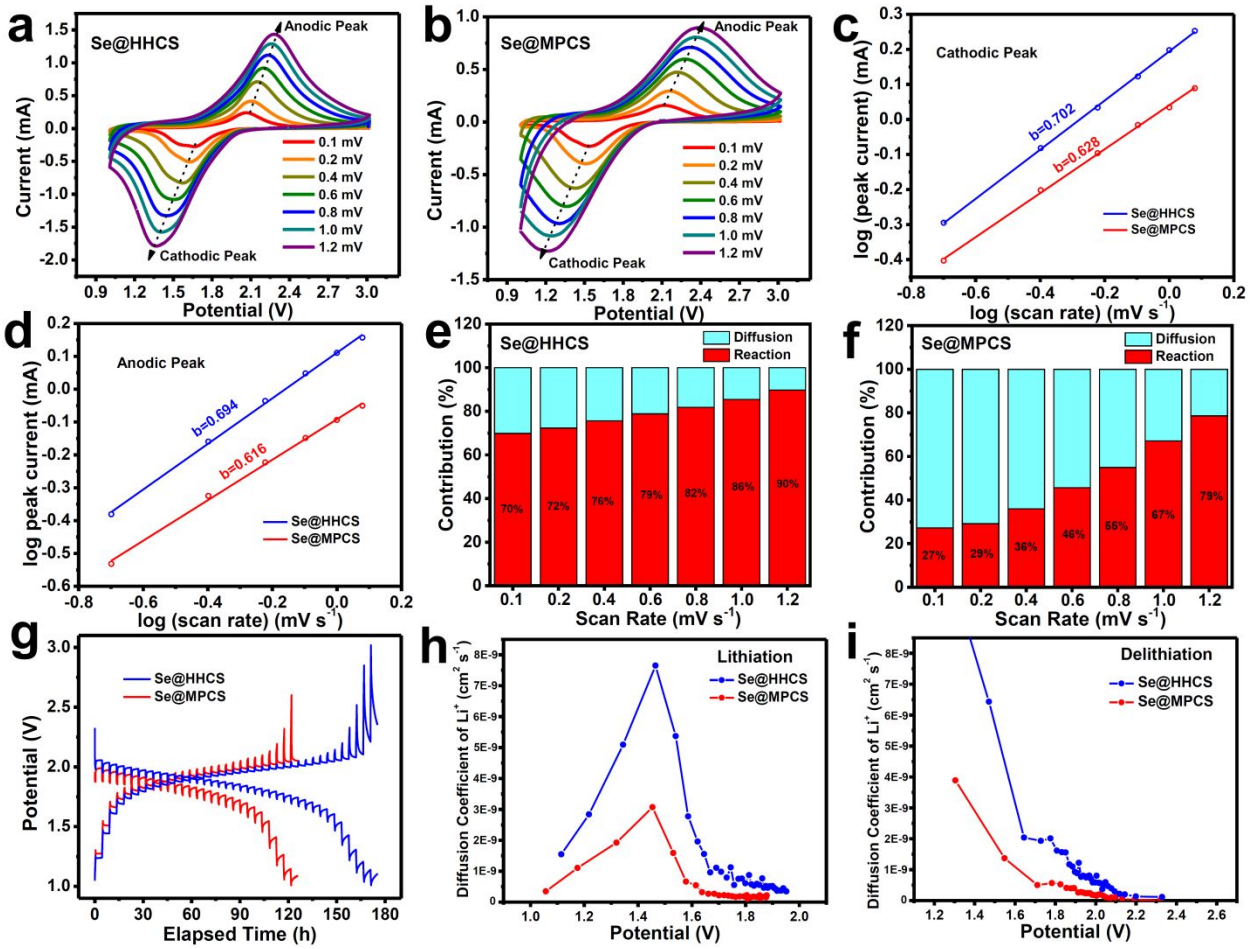

Figure 5. Electrochemical kinetics analysis directly comparing Se@HHCS versus Se@MPCS. **(a)**, **(b)** CV curves at various scan rates for the two electrodes. **(c)**, **(d)** Corresponding log(i) vs log(v) plots for cathodic and anodic peaks, respectively. **(e)**, **(f)** Reaction-controlled versus diffusion-controlled contribution to the total capacity at different scan rates for the two electrodes. **(g)** Comparison of GITT curves after 5 activation cycles. Current of 0.05C (34 mA g^{-1}) was applied for 0.5 h followed by a 4 h relaxation. **(h)**, **(i)** Comparison of Li^+ diffusion coefficients calculated from GITT analysis of lithiation and delithiation, respectively.

As shown in **Figures 5(c)** and **(d)**, $\boldsymbol{b}$ value can be obtained from the slope of the linear plots consisting of logarithmic peak currents $vs.$ scan rates. The fitted results show that the $\boldsymbol{b}$ values of Se@HHCS and Se@MPCS are 0.702 and 0.628 in terms of cathodic peaks, 0.694 and 0.616 for anodic peaks, both of which were between 0.5-1.0, indicating that the redox reactions were associated with both diffusion-controlled and reaction-controlled processes. The CV data are further analyzed using the formula $\boldsymbol{i(V) = k_1 v + k_2 v^{1/2}}$, where $\boldsymbol{k_1 v}$ represents the reaction-controlled contribution while $\boldsymbol{k_2 v^{1/2}}$ represents the diffusion-controlled contribution. As shown in **Figures 5(e) and 5(f)**, the reaction-controlled capacity contributions in both materials increase

with scan rate. The reaction-controlled contributions of the Se@HHCS cathode are 70%, 72%, 76%, 79%, 82%, 86% and 90% at the scan rates of 0.1, 0.2, 0.4, 0.6, 0.8, 1.0 and 1.2 mV s^{-1}, respectively. These values are higher than for Se@MPCS, where the associated percentages are 27%, 29%, 36%, 46%, 55%, 67% and 79%. This indicates that there are less diffusional limitations in Se@HHCS, agreeing with the hierarchical porosity arguments presented previously.

Galvanostatic intermittent titration technique (GITT) is an essential tool for investigating the ionic diffusivity through material where there is a single (or overwhelmingly dominant) ion active phase. The GITT plots of the Se@HHCS and Se@MPCS electrodes are displayed in **Figure 5(g)**. These were measured at a quasi-equilibrium current of 0.05C for 0.5 h during each pulse, followed by a 4 h relaxation to approach the steady state. Both electrodes were pre-cycled 5 times to stabilize the SEI and eliminate the side reactions before the GITT tests. The calculated diffusion coefficients of Li^+ (D_{Li^+}) during lithiation and delithiation are shown in **Figures 5(h) and 5(i)**, respectively. The D_{Li^+} values of both processes are in the range from 10^{-8} to 10^{-10} cm^2 s^{-1}. Se@HHCS possesses significantly higher diffusion coefficients in both lithiation and the delithiation processes, directly supporting the major differences in the fast-charging kinetics. As discussed previously, we argue that the remnant open nanoporosity in Se@HHCS is directly responsible for the increased diffusivity, with the electrolyte penetrated volume and the carbon - SEI interfaces providing complementary fast charge paths.

Conclusions

Lithium metal batteries based on a selenium cathode offer a promising volumetric energy but are limited in their fast charge and cycling capability. Much of the performance characteristics of any selenium-based cathode rests with the structure/chemistry of the carbon host, employed to maintain a nanoscale microstructure, buffer the repeated expansion - contraction and potentially prevent polyselenide crossover. Here, selenium is hosted in hierarchically porous hollow carbon spheres with remnant nanoporosity, which allows for exceptional fast charge and cycling performance in generic carbonate electrolyte without secondary additives. A broad comparison with state-of-the-art prior work indicates highly favorable performance of Se@HHCS in both respects. Two baselines were tested to further understand the role of the optimized hierarchically porous carbon host. In addition, post-mortem analysis was performed on the cycled electrodes. It

is demonstrated that the solid-state ionic diffusivity in Se@HHCS in 2-3 times higher than in the baseline at every state of charge, and that the electrode undergoes minimal distortion as a result of cycling. It is argued that both the rate capability and the cycling stability are directly related to the host's unique pore structure before and following selenium infiltration.

ACKNOWLEDGMENTS

D.M. Y.W., H.H. D.D. and P.L. (conception and guidance of research, syntheses and electrochemical analysis, preparation of the manuscript) were supported by the National Science Foundation, Civil, Mechanical and Manufacturing Innovation (CMMI), Award Number 1911905. This research used resources of the Center for Functional Nanomaterials (CFN), which is a U.S. Department of Energy Office of Science User Facility, at Brookhaven National Laboratory under Contract No. DE-SC0012704.

References

1. A. Singh and V. Kalra, *J. Mater. Chem. A*, 2019, **7**, 11613-11650.
2. D. Lin, Y. Liu and Y. Cui, *Nat. Nanotechnol.*, 2017, **12**, 194-206.
3. C. Yang, K. Fu, Y. Zhang, E. Hitz and L. Hu, *Adv. Mater.*, 2017, **29**, 1701169.
4. H. Huo, J. Gao, N. Zhao, D. Zhang, N. G. Holmes, X. Li, Y. Sun, J. Fu, R. Li, X. Guo and X. Sun, *Nat. Commun.*, 2021, **12**, 176.
5. C. Fang, X. Wang and Y. S. Meng, *Trends Chem.*, 2019, **1**, 152-158.
6. K. R. Adair, M. N. Banis, Y. Zhao, T. Bond, R. Li and X. Sun, *Adv. Mater.*, 2020, **32**, 2002550.
7. X. Wang, Y. Tan, Z. Liu, Y. Fan, M. Li, H. A. Younus, J. Duan, H. Deng and S. Zhang, *Small*, 2020, **16**, 2000266.
8. M. Zhao, B. Q. Li, X. Q. Zhang, J. Q. Huang and Q. Zhang, *ACS Cent. Sci.*, 2020, **6**, 1095-1104.
9. M. Zheng, Y. Chi, Q. Hu, H. Tang, X. Jiang, L. Zhang, S. Zhang, H. Pang and Q. Xu, *J. Mater. Chem. A*, 2019, **7**, 17204-17241.
10. C. Xia, C. Y. Kwok and L. F. Nazar, *Science*, 2018, **361**, 777-781.

11. J. Lai, Y. Xing, N. Chen, L. Li, F. Wu and R. Chen, *Angew. Chem. Int. Ed.*, 2020, **59**, 2974-2997.
12. T. Liu, J. P. Vivek, E. W. Zhao, J. Lei, N. Garcia-Araez and C. P. Grey, *Chem. Rev.*, 2020, **120**, 6558-6625.
13. G. Li, Z. Chen and J. Lu, *Chem*, 2018, **4**, 3-7.
14. Y. Hu, W. Chen, T. Lei, Y. Jiao, J. Huang, A. Hu, C. Gong, C. Yan, X. Wang and J. Xiong, *Adv. Energy Mater.*, 2020, **10**, 2000082.
15. Y. He, Z. Chang, S. Wu and H. Zhou, *J. Mater. Chem. A*, 2018, **6**, 6155-6182.
16. C. Luo, Y. Xu, Y. Zhu, Y. Liu, S. Zheng, Y. Liu, A. Langrock and C. Wang, *ACS Nano*, 2013, **7**, 8003-8010.
17. C. P. Yang, S. Xin, Y. X. Yin, H. Ye, J. Zhang and Y. G. Guo, *Angew. Chem. Int. Ed.*, 2013, **52**, 8363-8367.
18. Y. Qu, Z. Zhang, S. Jiang, X. Wang, Y. Lai, Y. Liu and J. Li, *J. Mater. Chem. A*, 2014, **2**, 12255-12261.
19. X. Gao, X. Yang, S. Wang, Q. Sun, C. Zhao, X. Li, J. Liang, M. Zheng, Y. Zhao, J. Wang, M. Li, R. Li, T. Sham and X. Sun, *J. Mater. Chem. A*, 2020, **8**, 278-286.
20. Y. Cui, A. Abouimrane, C. J. Sun, Y. Ren and K. Amine, *Chem. Commun.*, 2014, **50**, 5576-5579.
21. Z. Li, L. Yuan, Z. Yi, Y. Liu and Y. Huang, *Nano Energy*, 2014, **9**, 229-236.
22. Y. Liu, L. Si, X. Zhou, X. Liu, Y. Xu, J. Bao and Z. Dai, *J. Mater. Chem. A*, 2014, **2**, 17735-17739.
23. M. Kotkata and K. Kandil, *Mater. Sci. Eng.*, 1987, **95**, 287-293.
24. F. A. Perras, S. Hwang, Y. Wang, E. C. Self, P. Liu, R. Biswas, S. Nagarajan, V. H. Pham, Y. Xu, J. A. Boscoboinik, D. Su, J. Nanda, M. Pruski and D. Mitlin, *Nano Lett.*, 2020, **20**, 918-928.
25. J. Ding, H. Zhou, H. Zhang, T. Stephenson, Z. Li, D. Karpuzov and D. Mitlin, *Energy Environ. Sci.*, 2017, **10**, 153-165.
26. Q. Li, H. Liu, Z. Yao, J. Cheng, T. Li, Y. Li, C. Wolverton, J. Wu and V. P. Dravid, *ACS Nano*, 2016, **10**, 8788-8795.
27. A. Abouimrane, D. Dambournet, K. W. Chapman, P. J. Chupas, W. Weng and K. Amine, *J. Am. Chem. Soc.*, 2012, **134**, 4505-4508.

28. J. Ding, H. Zhou, H. Zhang, L. Tong and D. Mitlin, *Adv. Energy Mater.*, 2018, **8**, 1701918.
29. X. Gu, T. Tang, X. Liu and Y. Hou, *J. Mater. Chem. A*, 2019, **7**, 11566-11583.
30. J. Jin, X. Tian, N. Srikanth, L. B. Kong and K. Zhou, *J. Mater. Chem. A*, 2017, **5**, 10110-10126.
31. J. Sun, Z. Du, Y. Liu, W. Ai, K. Wang, T. Wang, H. Du, L. Liu and W. Huang, *Adv. Mater.*, 2021, **33**, 2003845.
32. S. Kim, M. Cho and Y. Lee, *Adv. Energy Mater.*, 2019, **10**, 1903477.
33. F. Zhang, X. Guo, P. Xiong, J. Zhang, J. Song, K. Yan, X. Gao, H. Liu and G. Wang, *Adv. Energy Mater.*, 2020, **10**, 2000446.
34. H. Tian, H. Tian, S. Wang, S. Chen, F. Zhang, L. Song, H. Liu, J. Liu and G. Wang, *Nat. Commun.*, 2020, **11**, 5025.
35. C. Zheng, M. Liu, W. Chen, L. Zeng and M. Wei, *J. Mater. Chem. A*, 2016, **4**, 13646-13651.
36. X. Zhao, L. Yin, T. Zhang, M. Zhang, Z. Fang, C. Wang, Y. Wei, G. Chen, D. Zhang, Z. Sun and F. Li, *Nano Energy*, 2018, **49**, 137-146.
37. C. Luo, J. Wang, L. Suo, J. Mao, X. Fan and C. Wang, *J. Mater. Chem. A*, 2015, **3**, 555-561.
38. W. Jin, H. Li, J. Zou, S. Inguva, Q. Zhang, S. Zeng, G. Xu and X. Zeng, *J. Alloys Compd.*, 2020, **820**, 153084.
39. W. Jin, H. Li, J. Zou, S. Inguva, Q. Zhang, S. Zeng, G. Xu and X. Zeng, *Mater. Lett.*, 2019, **252**, 211-214.
40. K. Han, Z. Liu, H. Ye and F. Dai, *J. Power Sources*, 2014, **263**, 85-89.
41. X. Wang, Z. Zhang, Y. Qu, G. Wang, Y. Lai and J. Li, *J. Power Sources*, 2015, **287**, 247-252.
42. D. Dutta, S. Gope, D. S. Negi, R. Datta, A. K. Sood and A. J. Bhattacharyya, *J. Phys. Chem. C*, 2016, **120**, 29011-29022.
43. S. Xin, L. Yu, Y. You, H. P. Cong, Y. X. Yin, X. L. Du, Y. G. Guo, S. H. Yu, Y. Cui and J. B. Goodenough, *Nano Lett.*, 2016, **16**, 4560-4568.
44. J. Zhang, Z. Zhang, Q. Li, Y. Qu and S. Jiang, *J. Electrochem. Soc.*, 2014, **161**, A2093-A2098.

45. Y. Liu, L. Si, Y. Du, X. Zhou, Z. Dai and J. Bao, *J. Phys. Chem. C*, 2015, **119**, 27316-27321.
46. L. Zeng, X. Wei, J. Wang, Y. Jiang, W. Li and Y. Yu, *J. Power Sources*, 2015, **281**, 461-469.
47. S. Park, J. Park and Y. C. Kang, *J. Mater. Chem. A*, 2018, **6**, 1028-1036.
48. R. Mukkabla, Kuldeep and M. Deepa, *ACS Appl. Energy Mater.*, 2018, **1**, 6964-6976.
49. R. Mukkabla, S. Deshagani, P. Meduri, M. Deepa and P. Ghosal, *ACS Energy Lett.*, 2017, **2**, 1288-1295.
50. Y. Lai, F. Yang, Z. Zhang, S. Jiang and J. Li, *RSC Adv.*, 2014, **4**, 39312-39315.
51. J. Zhang, L. Fan, Y. Zhu, Y. Xu, J. Liang, D. Wei and Y. Qian, *Nanoscale*, 2014, **6**, 12952-12957.
52. J. Guo, Z. Wen, G. Ma, J. Jin, W. Wang and Y. Liu, *RSC Adv.*, 2015, **5**, 20346-20350.
53. J. Guo, Q. Wang, C. Qi, J. Jin, Y. Zhu and Z. Wen, *Chem. Commun.*, 2016, **52**, 5613-5616.
54. T. Liu, C. Dai, M. Jia, D. Liu, S. Bao, J. Jiang, M. Xu and C. M. Li, *ACS Appl. Mater. Interfaces*, 2016, **8**, 16063-16070.
55. P. Xue, Y. Zhai, N. Wang, Y. Zhang, Z. Lu, Y. Liu, Z. Bai, B. Han, G. Zou and S. Dou, *Chem. Eng. J.*, 2020, **392**, 123676.
56. J. K. Kim and Y. C. Kang, *ACS Nano*, 2020, **14**, 13203-13216.
57. H. Zhang, L. Zhou, X. Huang, H. Song and C. Yu, *Nano Res.*, 2016, **9**, 3725-3734.
58. B. Kalimuthu and K. Nallathamby, *ACS Appl. Mater. Interfaces*, 2017, **9**, 26756-26770.
59. G. D. Park, J. H. Kim, J. Lee and Y. Chan Kang, *J. Mater. Chem. A*, 2018, **6**, 21410-21418.
60. R. Pongilat and K. Nallathamby, *J. Phys. Chem. C*, 2019, **123**, 5881-5889.
61. Y. J. Hong and Y. C. Kang, *Carbon*, 2017, **111**, 198-206.
62. Y. Lei, X. Liang, L. Yang, P. Jiang, Z. Lei, S. Wu and J. Feng, *J. Mater. Chem. A*, 2020, **8**, 4376-4385.
63. W. Dong, H. Chen, F. Xia, W. Yu, J. Song, S. Wu, Z. Deng, Z. Y. Hu, T. Hasan, Y. Li, H. Wang, L. Chen and B. L. Su, *J. Mater. Chem. A*, 2018, **6**, 22790-22797.
64. J. Zhou, J. Yang, Z. Xu, T. Zhang, Z. Chen and J. Wang, *J. Mater. Chem. A*, 2017, **5**, 9350-9357.
65. D. B. Babu and K. Ramesha, *Electrochim. Acta*, 2016, **219**, 295-304.
66. B. Kalimuthu and K. Nallathamby, *ACS Sustain. Chem. Eng.*, 2018, **6**, 7064-7077.

67. K. Han, Z. Liu, J. Shen, Y. Lin, F. Dai and H. Ye, *Adv. Funct. Mater.*, 2015, **25**, 455-463.
68. S. Lee, J. Lee, W. Kim, H.-J. Kim, C. Pak, J. T. Lee and K. Eom, *J. Power Sources*, 2018, **408**, 111-119.
69. L. Liu, Y. Wei, C. Zhang, C. Zhang, X. Li, J. Wang, L. Ling, W. Qiao and D. Long, *Electrochim. Acta*, 2015, **153**, 140-148.
70. J. Liu, S. Z. Qiao, H. Liu, J. Chen, A. Orpe, D. Zhao and G. Q. Lu, *Angew. Chem. Int. Ed.*, 2011, **50**, 5947-5951.
71. M. Lillo-Ródenas, D. Cazorla-Amorós and A. Linares-Solano, *Carbon*, 2003, **41**, 267-275.
72. J. Wang and S. Kaskel, *J. Mater. Chem.*, 2012, **22**, 23710-23725.
73. J. Pokrzywinski, J. K. Keum, R. E. Ruther, E. C. Self, M. Chi, H. Meyer Iii, K. C. Littrell, D. Aulakh, S. Marble, J. Ding, M. Wriedt, J. Nanda and D. Mitlin, *J. Mater. Chem. A*, 2017, **5**, 13511-13525.
74. Y. Lai, Y. Gan, Z. Zhang, W. Chen and J. Li, *Electrochim. Acta*, 2014, **146**, 134-141.
75. Y. Wang, W. Tian, L. Wang, H. Zhang, J. Liu, T. Peng, L. Pan, X. Wang and M. Wu, *ACS Appl. Mater. Interfaces*, 2018, **10**, 5577-5585.
76. Y. Wang, Y. Wang, J. Liu, L. Pan, W. Tian, M. Wu and J. Qiu, *Carbon*, 2017, **122**, 344-351.
77. K. Sing and R. Williams, *Adsorp. Sci. Technol.*, 2004, **22**, 773-782.
78. M. H. A. Shiraz, H. Zhu, Y. Liu, X. Sun and J. Liu, *J. Power Sources*, 2019, **438**, 227059.
79. Z. Yi, L. Yuan, D. Sun, Z. Li, C. Wu, W. Yang, Y. Wen, B. Shan and Y. Huang, *J. Mater. Chem. A*, 2015, **3**, 3059-3065.
80. X. Zhao, L. Yin, Z. Yang, G. Chen, H. Yue, D. Zhang, Z. Sun and F. Li, *J. Mater. Chem. A*, 2019, **7**, 21774-21782.
81. P. Zhao, M. H. A. Shiraz, H. Zhu, Y. Liu, L. Tao and J. Liu, *Electrochim. Acta*, 2019, **325**, 134931.
82. J. P. Song, L. Wu, W. D. Dong, C. F. Li, L. H. Chen, X. Dai, C. Li, H. Chen, W. Zou, W. B. Yu, Z. Y. Hu, J. Liu, H. E. Wang, Y. Li and B. L. Su, *Nanoscale*, 2019, **11**, 6970-6981.
83. L. Zeng, X. Chen, R. Liu, L. Lin, C. Zheng, L. Xu, F. Luo, Q. Qian, Q. Chen and M. Wei, *J. Mater. Chem. A*, 2017, **5**, 22997-23005.
84. J. He, Y. Chen, W. Lv, K. Wen, P. Li, Z. Wang, W. Zhang, W. Qin and W. He, *ACS Energy Lett.*, 2016, **1**, 16-20.

85. R. Qiu, R. Fei, T. Zhang, X. Liu, J. Jin, H. Fan, R. Wang, B. He, Y. Gong and H. Wang, *Electrochim. Acta*, 2020, **356**, 136832.
86. Y. Wang, B. Hou, J. Guo, Q. Ning, W. Pang, J. Wang, C. Lü and X. Wu, *Adv. Energy Mater.*, 2018, **8**, 1703252.
87. X. Yang, J. Wang, S. Wang, H. Wang, O. Tomanec, C. Zhi, R. Zboril, D. Y. W. Yu and A. Rogach, *ACS Nano*, 2018, **12**, 7397-7405.
88. Y. Yao, M. Chen, R. Xu, S. Zeng, H. Yang, S. Ye, F. Liu, X. Wu and Y. Yu, *Adv. Mater.*, 2018, **30**, 1805234.
89. Y. Sun, H. Wang, W. Wei, Y. Zheng, L. Tao, Y. Wang, M. Huang, J. Shi, Z. C. Shi and D. Mitlin, *ACS Nano*, 2021, **15**, 1652-1665.
90. L. Tao, Y. Yang, H. Wang, Y. Zheng, H. Hao, W. Song, J. Shi, M. Huang and D. Mitlin, *Energy Storage Mater.*, 2020, **27**, 212-225.